Combinatorial Performance Mapping of Near-NMC111 Li-ion Cathodes

Daniel Commandeur, Christian Sabado, Thomas E. Ashton, Jawwad A. Darr[*]

Department of Chemistry, University College London, 20 Gordon Street, London, WC1H 0AJ, UK

ARTICLE INFO

ABSTRACT

A combinatorial library of twenty-three, phase pure, near-NMC111 ($LiNi_{0.33}Mn_{0.33}Co_{0.33}O_2$) compositions were synthesised and their electrochemical performance, was mapped (in lithium ion half-cells). Each of the 23 compositions was made in series, using a two-step process of 1) a rapid initial continuous hydrothermal precipitation, followed by 2) solid state lithiation. The 23 lithiated NMC samples were then subjected to analytical methods including electron microscopy (selected samples), Powder X-ray Diffraction and electrochemical tests in half cell Li-ion configurations versus Li metal. A sample with a Ni:Mn:Co (NMC) ratio of 39:28:33, revealed a specific capacity of 150 mA h g^{-1} at a C/20 rate, which was 63 and 43% greater capacity than NMC111 and NMC433 samples produced in this work, respectively. The sample with NMC ratio 47:25:28, showed the best capacity retention characteristics, retaining 70% of its C/20 capacity at 1C, after 40 cycles. Further analysis of all the samples by cyclic voltammetry and electrochemical impedance spectroscopy, allowed compositional mapping of diffusion coefficients. Overall, the mapping data revealed a gradual change of properties across compositional space, which has validated our combinatorial approach and allowed identification of the optimum performing near-NMC111 cathode materials.

1. Introduction

In order to transition towards a low carbon future, our capacity to harness and store renewable energy, must improve [1]. Whether applied to Electric Vehicles (EVs) or smartphones, lithium ion batteries (LIBs) have become indispensable to modern life [2]. High power LIBs are crucial to future EVs and large-scale energy storage, although higher energy density cathodes are required to match the capacities offered by the newer anode materials [3,4]. The last two decades have seen the rise of layered cathodes such as $LiCoO_2$ (LCO) to prominence, storing energy by the intercalation of Li$^+$ between alternating layers of transition metal oxides [5,6]. Providing the benchmark for high power cathodes, LCO has been widely applied to EVs. However, lower cobalt content cathodes have been commercialised in order to offset the low capacity of LCO (~125 mA h g^{-1}) [7,8] as well as high material cost and ethical issues surrounding cobalt and its mining [9].

Energy dense layered cathodes have been made by incorporating nickel into the $R\bar{3}m$ structure, which provides higher capacities (~200 mA h g^{-1}) but this can suffer from instability and rapid degradation in its pure $LiNiO_2$ form [10]. The inclusion of further transition metals such as manganese, has improved long term structural stability and safety [11]. In contrast, cobalt has generally been added to these structures to improve rate capability [12]. Thus, NMC compositions (which include all three metals) can give rise to a balance of properties, which include improved safety, high energy density and fast charge capability [13–15]. Notable NMC compositions, which have been commercialised include $LiNi_{0.33}Mn_{0.33}Co_{0.33}O_2$ and $LiNi_{0.5}Mn_{0.3}Co_{0.2}O_2$ (also known as NMC111 and NMC532, respectively) [16]. Great progress has been made in increasing the degradation resistance of cathode active materials through coating with inert and lithium reactive species [17–20] doping and particle concentration gradients [21–25]. Challenges still remain to improve properties such as high power performance and stability under ever increasing energy densities [26]. Although there are a large number of reports covering the properties of specific NMC compositions, to the authors' knowledge, there appear to be no comprehensive combinatorial studies in the literature covering more than six samples each [27,28]. This is in part due to the difficulties in consistently preparing large numbers of subtly different lithiated NMC materials that is pre-requisite for electrochemical comparison.

---

* Corresponding author.
E-mail address: j.a.darr@ucl.ac.uk (J.A. Darr).
Peer review under responsibility of The Chinese Ceramic Society.

NMCs can be made *via* a number of methods, which are largely batch processes requiring a great deal of process control. These include coprecipitation, solid state, batch hydrothermal, sol-gel or various combustion methods [21,29–33]. When NMC cathodes are designed for high energy density, well packed, solid centred particles with sizes $\geq$ 10 μm are often used [4]. Consequently, such cathodes are often not evaluated at C-rates higher than 2C as they do not tend to have good capacity retention compared to the initial first cycle capacity [34–36]. Various efforts have been made to improve rate capability, to lower capacity losses at rates of 5C and higher. Huang et al. synthesised samples containing a Co concentration gradient that were Co-rich at the core and deficient at the surface, leading to 65% capacity retention at 10C compared to the initial first cycle capacity (195 mA h g^{-1} at C/5) [28]. Sun et al. coupled a concentration gradient secondary particle (6 μm secondary particle size) with nanostructured needle like constituent particles (2 μm length), giving 79% capacity retention at 5C [37].

To achieve high power performance in cathode materials, a small secondary particle size (a few microns or smaller) and high surface area can be used [38]. For example, batch coprecipitation has been refined via process control (pH, concentration and temperature) [39], to make complex microparticles in the size range 4–10 μm. Complex internal structure and high surface area) deliver enhanced lithium diffusion at high C-rates [40]. Zheng *et al.* demonstrated that 79% capacity retention was possible at 10C for NMC811 (compared to the initial cycle value at C/10), by optimising the lithiation/heat treatment temperature, reducing the size of primary particles to 100–300 nm [41]. One of the highest rate capabilities for NMC111 in literature was reported by Ren *et al.* in which 6 μm secondary particles were engineered with orientated diffusion channels, yielding a cathode with 89% retention at 10C (compared to the initial cycle value at C/5) [16].

Herein, we report the focussed synthesis of twenty-three near-NMC111 compositions and their analytical and electrochemical evaluation (within lithium ion half-cells); from NMC111 (metal ratio 33:33:33) to NMC211 (metal ratio 50:25:25). The systematic approach produced phase pure materials in all cases that allowed structure-property-compositional mapping and identification of an optimum high power, stable, high energy NMC composition. Furthermore, using our high-throughput synthetic methodology, the different precursor compositions (pre-lithiation) were made within a couple of hours, giving a considerable time saving compared to more conventional or batch hydrothermal synthesis methods.

2. Results and discussion

2.1. Structure and morphology

The precursor slurries obtained in series from the Continuous Hydrothermal Flow Synthesis (CHFS) process, appeared dark brown in colour when wet and were jet-black (free flowing) powders after freeze drying. Yields were in the range 68–78% (due to small samples sizes and losses from unoptimised workups), giving ca. 15g for each of the 23 samples in the library. After all samples had each individually undergone solid-state lithiation, they appeared to have a blue-grey colour and were gritty, necessitating gentle hand grinding for a few minutes to obtain relatively fine flowing powders.

In order to confirm the structure and phase purity of samples in the library, each sample was separately analysed using Powder X-ray Diffraction (PXRD). An example pattern of the NMC111 sample is displayed in Fig. 1a, which was indexed as the expected $R\overline{3}m$ layered structure of LiNi$_x$Mn$_y$Co$_z$O$_2$ (ICSD collection code 99,890)

[42]. No evidence of any impurity phases were found in any of the 23 samples produced. Fig. 1 b shows magnified plots of (003) and (110) peaks for materials with increasing Ni content, where [Mn] = [Co]. A peak shift to lower 2θ was only observed in the (110) peak upon increasing [Ni] in the powder. This is likely due to the larger ionic radius of Ni^{2+} (0.69 Å), the majority charge state of Ni in the material [43]. In contrast, Fig. 1 c shows the (003) and (110) peaks for samples where the Mn:Co ratio varied with a fixed Ni value of (Ni fixed at ca. 44 to 45% of total transition metal concentration). Again, a peak shift to lower 2θ was observed, but in both the (003) and (110) reflections.

To investigate these differences further, the lattice parameters of each sample were calculated using the unit cell equation for the R-3m space group.

From Fig. 1, clear changes in lattice parameters were observed as the ratio of metals in NMC were varied. Fig. 1c) shows that increasing the Mn:Co ratio (fixed Ni value of ca. 44 to 45% wrt total metal content) led to a monotonic expansion of parameter *a* and larger *c* values, due to the larger ionic radius of Mn^{3+} (0.65 Å compared to 0.545 and 0.56 Å for Co^{3+} and Ni^{3+}, respectively) [44]. When the Mn:Co ratio was maintained near to unity (range 0.96 to 1.03) and the Ni content increased from 0.34 to 0.46, the *a* parameter increased from 5.847 to 5.850 Å. This was likely due to the presence of more Ni^{2+} that has a larger radius (0.69 Å) than Ni^{3+}. This would be expected to distort the lattice outward along the TM layer plane, whereas a slight contraction is seen on the interlayer *c* axis parameter. Arguably this may be due to the Ni^{2+} occupying spaces in the alternating lithium layers through the phenomenon of cation mixing (which can also limit the potential active sites for lithium causing capacity fade). This cation mixing is possible due to the similar ionic radii of Ni^{2+} and Li$^+$ at 0.69 and 0.76 Å, respectively [18,45].

A previous report by Gao *et al.* suggested that the intensity ratio of the (003) to the (104) peaks (I$_{003}$/I$_{104}$) for NMC111, could qualitatively suggest the extent of cation mixing [46]. The higher the I$_{003}$/I$_{104}$ ratio, the lower the extent of cation mixing, with a ratio near to 1.2 believed to minimise this effect. The I$_{003}$/I$_{104}$ ratio of NMC 111 was 1.04, lower than the ideal value, but reasonable considering the heat-treatments were performed in static air [9]. Heat-treatments in an oxygen rich environment, or with a dynamic flow of air, can provide higher partial pressure of oxygen for the lithiation reaction, requiring less harsh lithiation conditions, which can limit cation mixing [47].

To identify the effect of elemental composition on cation mixing more thoroughly, the elemental compositions of the samples were determined by X-Ray Fluorescence (XRF) and plotted against the I$_{003}$/I$_{104}$ peak ratios in the ternary diagram, Fig. 2a); specific NMC compositions of NMC 111, 433, 532 and 622 are also highlighted as compositional markers. For clarity, a magnified view focussing on the compositions made herein, is provided in Fig. 2b). A trend can be seen with increasing concentration of nickel; cation mixing appears to increase (I$_{003}$/I$_{104}$ peak ratios reducing to 0.96 for NMC 45:35:25). This might be explained by the fact that a greater quantity of Ni^{2+} leads to more migration into the lithium layers due to size similarities; in nickel-rich cathodes, this problem can often be alleviated by heat-treatment in O$_2$ [24]. Conversely, it was observed that cation mixing seemed to reduce for samples, which contained high levels of cobalt (I$_{003}$/I$_{104}$ reached a maximum of 1.10 for the NMC 48:22:31 sample). This was likely to be due the role of cobalt in the layered structure, relieving the magnetic frustration of spin aligned Ni^{3+} ions. These ions have a relatively strong magnetic moment and although this can be relieved by anti-alignment, when arranged in the $R\overline{3}m$ lattice, they are arranged triangularly. Therefore, there will always be neighbouring ions that are aligned, in a
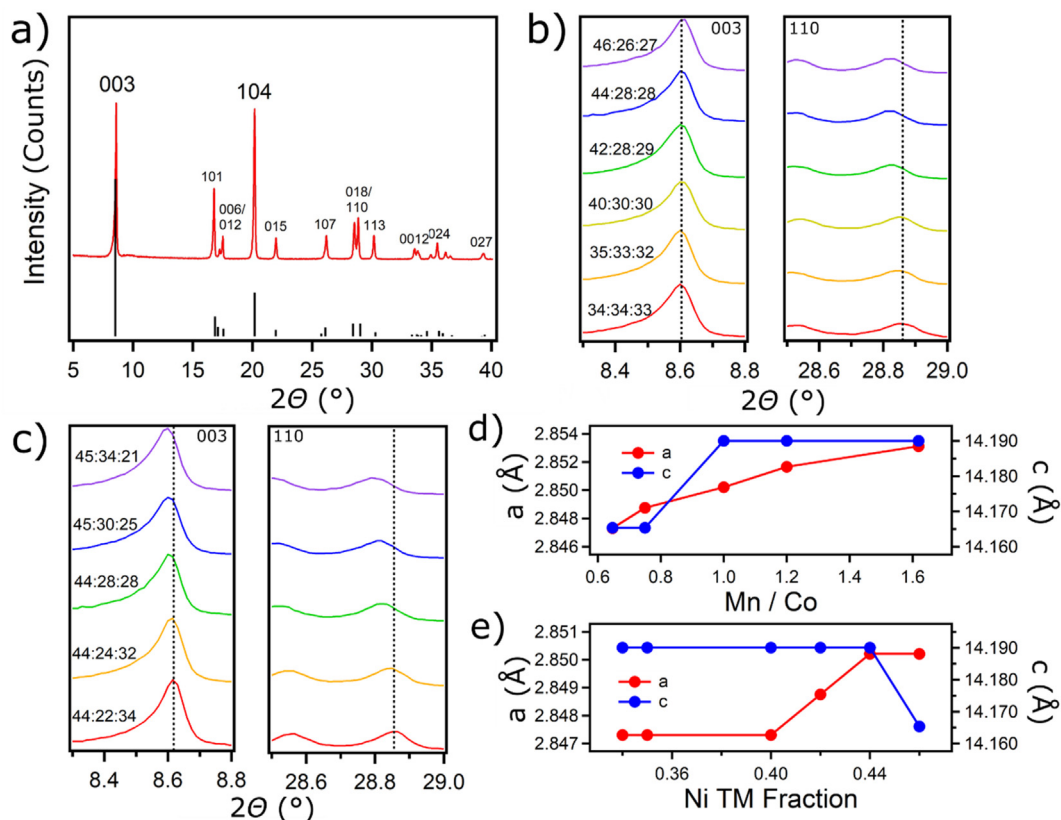
D. Commandeur, C. Sabado, T.E. Ashton et al.

Fig. 1. a) PXRD for the NMC 111 sample from the library with indexed peaks labelled (003 and 104) that were used to determine cation mixing. b) Magnified view of (003) and (104) PXRD peaks for selected samples with near equal Mn:Co ratio and differing Ni values. c) Magnified view of the same peaks for samples with approximately fixed Ni concentration and a differing Mn:Co ratios. d) a and c lattice parameter values versus the Mn/Co fraction values (at fixed Ni value of ca. 44 to 45% Ni in NMC). e) a and c lattice parameter values versus Ni fraction in the NMC (where Mn/Co values were in the narrow range 0.96 to1.03).
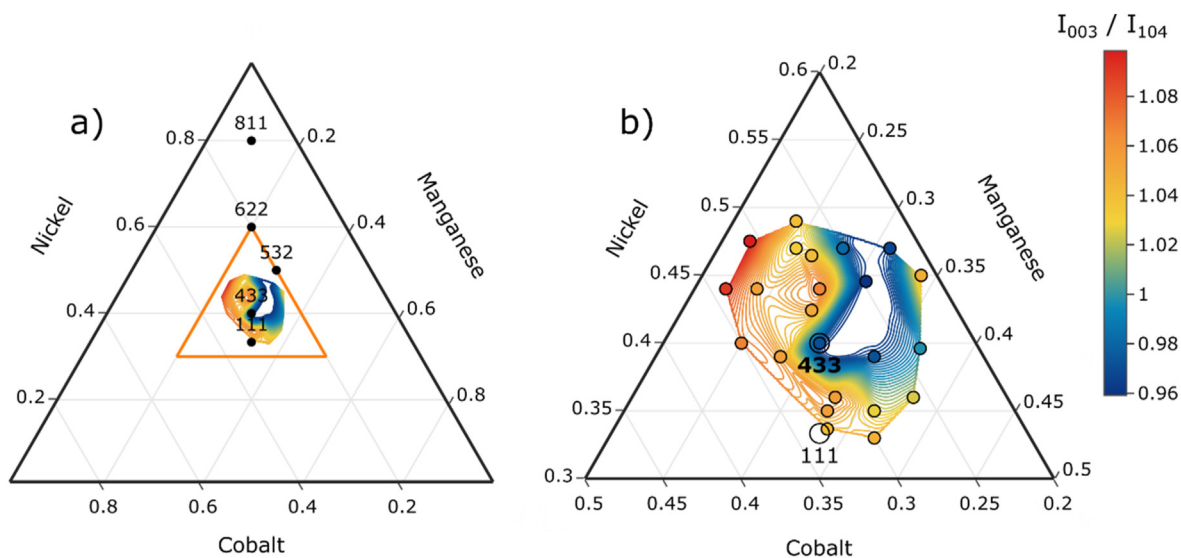

Fig. 2. a) Shows a ternary plot of and expanded compositional range, with common NMC compositions plotted. b) Shows the magnified central region, with the XRF determined compositions plotted with I_{003}/I_{104} peak ratio (represented by colour of dot).

higher energy state. Cation mixing occurs as Li^+ ions have no spin, therefore, they can easily relieve this magnetic frustration by exchanging with Ni^{3+}. Although, as nickel, cobalt is a ferromagnetic material, Co^{3+} ions have no spin and therefore, no magnetic moment. By increasing the concentration of Co^{3+}, less Li^+ migrates

into the nickel sites to relieve magnetic frustration during lithiation and cycling [12]. Though Mn^{3+} should too have this effect in such systems, there is likely a significant prevalence of Mn^{4+} in the samples [48], which would be expected to exacerbate magnetic frustration; hence, it may not have behaved like the cobalt [9]. The

effect of Co/Mn ratio on cation mixing, followed the trend where larger quantities of Mn, led to greater abundance of NiLi. This effect has been previously predicted by Yin et al. in a study where high precision powder diffraction was applied to study a range of NMC compositions and their defect concentration [49]. Their model calculated that the NiLi concentration showed an increasing trend towards greater quantities of Mn on a ternary plot, moving outward from NMC 111, as observed in the ternary space in the present study.

Thus, prior to electrochemical testing, it might be expected that better rate capability and capacity at low rates, would be observed for samples with lower cation mixing.

In order to achieve high rate capability in NMC cathodes, it is desirable to be able to manufacture these materials below 3 μm in size, where the high surface area could facilitate more rapid lithium intercalation and deintercalation [50]. The particle morphology of selected samples in the library, was studied using Scanning Electron Microscopy (SEM), see Fig. 3. SEM images of the NMC 45:31:25 sample are shown in low magnification Fig. 3a), followed by increasing magnification for Fig. 3b) and c). The same magnification in c) is shown for samples 34:34:33 in Fig. 3d), NMC 35:36:29 in Fig. 3e) and sample NMC 40:30:30 in Fig. 3f).

In Fig. 3a) the NMC 45:31:25 sample was found to consist of microparticles in the size range 0.8 to 10.1 μm (averaging 4.0 ± 1.8 μm) [100 particle measurements per sample]. This was comparable across all the samples characterised by SEM, including NMC 34:34:33 (4.3 ± 1.7 μm); NMC 35:36:29 (3.8 ± 1.9 μm) and NMC 40:30:30 (3.5 ± 1.9 μm), low magnification images are shown in Fig. S1. At higher magnification for sample NMC 45:31:25, it was more evident that these structures were assemblies of particles with a size range of 150 to 660 nm (average 320 ± 80 nm). Such primary particle size is likely due to the small size of the precursor oxides made using CHFS, which limited particle growth and sintering during the lithiation heat-treatment [51]. A report by Zheng et al., also suggested that for NMC811, such a small primary particle size might enhance high power performance [41]. This is because higher surface area will allow more rapid intercalation of lithium, due to minimized diffusion distances and greater contact with the electrolyte [52].

SEM images obtained herein, appear to show highly uniform particles across compositional space. High magnification SEM images for samples NMC111(34:34:33), NMC 35:36:29 and NMC433 are shown in Fig. 3d), e) and 3f), respectively. Analysis of the images suggest a primary particle size in the range 150 to 620 nm for sample NMC111 (34:34:33) [average 320 ± 107 nm]. For the NMC 35:36:29 and NMC433 samples, primary particles were in the range from 150 to 590 nm (average 280 ± 90 nm) and 170−700 nm (average 370 ± 110 nm), respectively.

The particle sizes were also estimated by Scherrer analysis of the (003) peak from powder XRD, Table S2 [53]. The sizes show little variation across compositional space, being in the range 28 to 35 nm. This implies that across this range the composition plays a small role in determining the particle size, this is more greatly affected by conditions of heat treatment. These values are also an order of magnitude lower than the primary particles measured by SEM. This is likely due to the particle size limitation of Scherrer analysis, these particles are likely too large for significant peak broadening [54]. Furthermore, the primary particles may not be single crystal domains and likely contain crystal defects that will affect the full width half maximum of the pattern peaks [55].

2.2. Li-ion half cell performance

Electrochemical investigations including Galvanostatic Charge Discharge (GCD) cycling, were performed on the library of cathodes in lithium ion half cells, see Fig. 4. Charge and discharge data for the highest capacity sample NMC 39:28:33, are shown in Fig. 4a), with C-rates in the range C/20 to 1C (specific capacities given in Table S3). In the initial cycles for sample NMC 39:28:33 at C/20, a specific capacity of 150 mA h g^{-1} was observed with low coulombic efficiency (presumably due to the formation of the SEI layer) [56]. This capacity is similar to that expected for analogous NMC literature materials which are typically in the range 140 to 170 mA h g^{-1} for NMC111 [22,31,57,58], and ca. 165 mA h g^{-1} for NMC433 (at low C rates) [59].

Fig. 4c) maps the capacities of the electrodes at C/20 across compositional space, which are in the range 92 to 150 mA h g^{-1} (capacity values are listed in Supplementary Table S3). Following an
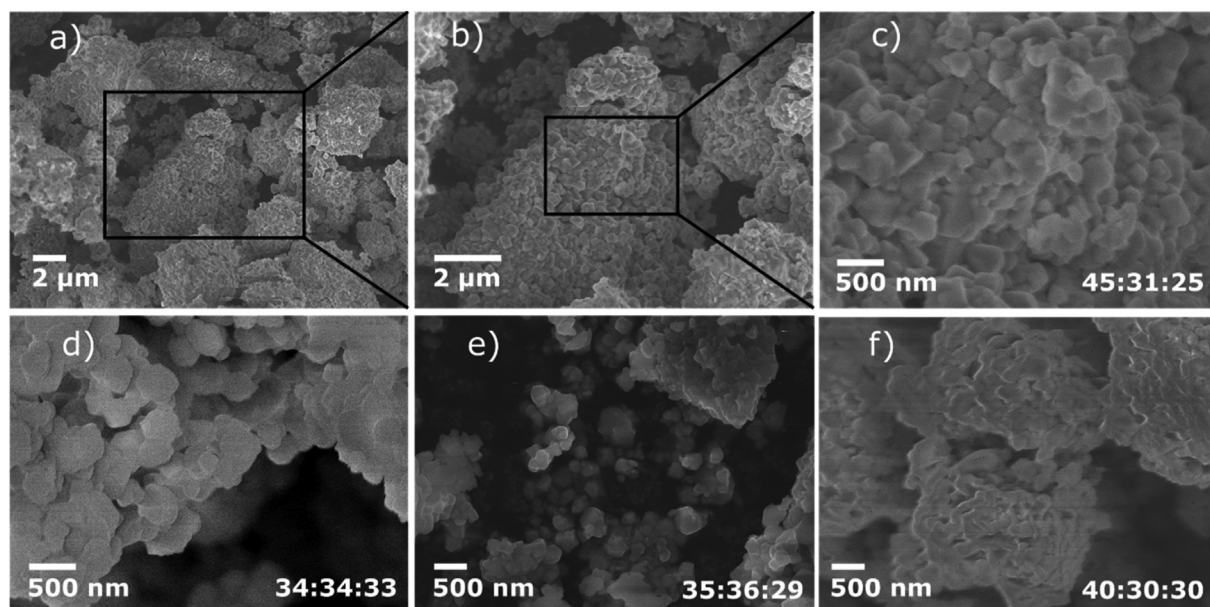

Fig. 3. SEM images of the NMC 45:31:25 sample are shown in low magnification a), followed by increasing magnification for b) and c). The same magnification in c) is shown for samples NMC 34:34:33 in d); NMC 35:36:29 in e) and NMC 40:30:30 in f).
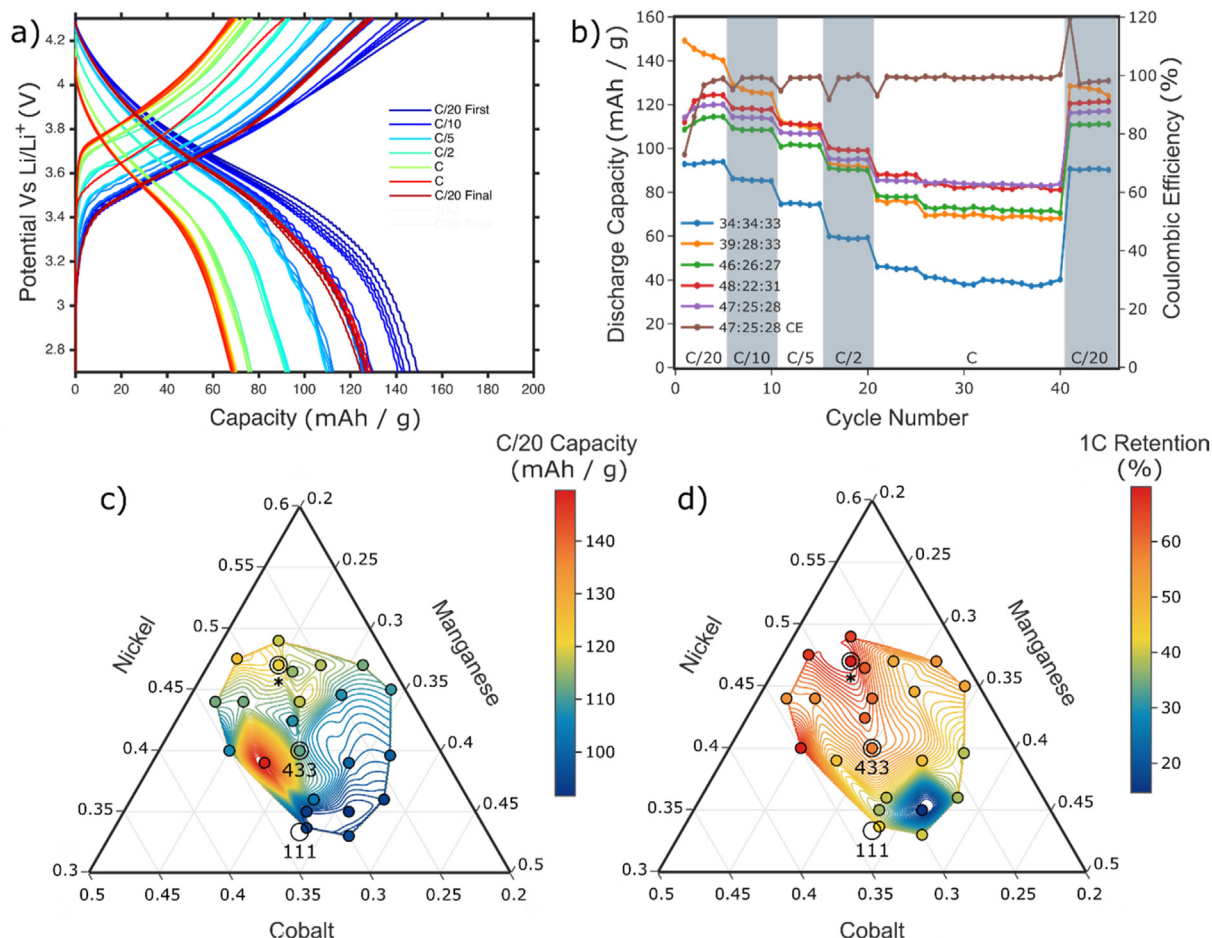
Fig. 4. a) Shows the charge discharge curves for the highest C/20 capacity sample, NMC 39:28:33. b) Shows the discharge capacities of several samples for comparison, including the coulombic efficiency for the highest 1C sample, NMC 47:25:28. c) Compares the C/20 capacities across the ternary compositional space, whilst the 10C capacity retention is compared in d). The high-power sample NMC 47:25:28 is highlighted by *.

approximately vertical path up through compositional space on the C/20 capacity map (increasing Ni levels), the capacity values were in the range 94 mA h g^{-1} (for NMC 34:34:33) to 118 mA h g^{-1} (for NMC 49:24:27). Furthermore, at higher nickel contents, the presence of more cobalt was advantageous for obtaining a high capacity (observed in NMCs 49:24:27, 48:22:31, 47:25:28), giving a capacity of 125 mA h g^{-1} for sample NMC 48:22:31 (at C/20). In comparison, sample NMC 47:31:22 (with the cobalt and manganese contents, swapped compared to sample NMC 48:22:31) and achieved a lower capacity of 113 mA h g^{-1}. As previously mentioned, sample NMC 39:28:33 achieved a reasonable capacity of 150 mA h g^{-1} but many of the other samples were slightly lower than expected (typical range expected was ca. 140 to 170 mA h g^{-1} for NMC111 at C/20) [22,31,57,58]. However, this is unsurprising. given that electrodes were not calendared or optimised in the initial fast screening stage.

The rate performance of the samples across the library at different C-rates, was also assessed. Sample NMC 39:28:33 showed a big drop in capacity at higher C rates, giving 69 mA h g^{-1} at 1C (53% loss compared to the initial cycle value at C/20). The rate capabilities of other NMC library samples are displayed in Fig. 4b); samples with higher Ni content such as NMC 46:26:27, NMC 48:22:31 and NMC 47:25:28, achieved capacities of 72, 83 and 84 mA h g^{-1} at 1C, respectively. These results were consistent with the suggestion that increased cobalt content would lead to greater rate capability [11]. Furthermore, it was found that sample NMC 47:25:28 showed excellent capacity retention (ca. 84 mA h g^{-1} that

was ca. 70% of its initial C/20 performance) after 20 cycles at 1C (see Fig. 4d).

It has been widely acknowledged that the three transition metals in NMC, offer different advantages for the cathode material [2–4]. Higher nickel content is associated with greater capacity and therefore, energy density, whilst greater rate capability and capacity retention, is attributed to having more cobalt [5]. This study affirms these observations in the near NMC111 region, where a general trend of increased capacity with higher Ni content, was measured. Furthermore, increased Co content, generally led to greater capacity retention at higher rates of charge. Finally, manganese is known to have a positive effect on safety and thermal stability; the confirmation of this benefit is outside the scope of this study, though this may prove a fruitful avenue of future research [6].

Sample NMC 47:25:28 was calculated to deliver a power density of 6148 W kg^{-1} at an energy density of 314 Wh kg^{-1} [see Fig. S2a], contour plot of power density]. Adding more Ni to this optimum composition, only reduced the capacity retention at 1C (C/20 energy densities are plotted in Fig. S2b).

The outstanding high rate capacity retention of sample NMC 47:25:28 will require optimisation of heat treatment conditions to match higher C-rate capacity NMCs in literature, such as in the report by Huang et al. on NMC 70:15:15 (65% retention at 10C with a capacity of 115 mA h g^{-1}) [60], or NMC811 (55% retention at 10C with a capacity of 100 mA h g^{-1}) [61], NMC111 (20% retention at 8C

D. Commandeur, C. Sabado, T.E. Ashton et al.

or 57% retention at 10C) [16,26]. The bottom-up synthetic method presented here, also lends itself to additional particle engineering, such as the strategy employed by Ren *et al.* to make highly orientated NMC 111, revealing an impressive 86% retention at 10C [16]. This composition also matches in situ XRD and thermal stability studies on various commercial NMC ratios that were reported by Bak et al.; NMC 532 was found to be the best trade-off for high stability and high capacity in comparison to NMC 622, 811 and 433 [62].

The cycling stability of the samples was determined by finding the percentage reduction in capacity from the first cycle to the 45th cycle; both these cycles used a current density of C/20. The results are displayed in Table S3 and are mapped against composition in Fig. S3. NMC433 was found to have the highest stability, showing no measurable degradation after 45 cycles. In this work, with nickel content below 50%, all samples showed good cycling stability, with the optimum high-power sample NMC 47:25:28, fading by just 2.5%. This active material will require further cycling in the future to confirm its long-term stability behaviour.

2.3. Diffusion and SEI formation

In order to further understand the effect of composition on the electrochemical properties of the NMC samples, Cyclic Voltammetry (CV) was performed on all the samples. The CV of the sample NMC 39:28:33 at 0.1 mV s^{-1} scan rate (Fig. 5a), displayed a single redox couple, with peaks centred at 3.97 V (delithiation) and 3.80 V (lithiation) vs Li/Li$^+$. This corresponded to the Ni^{2+}/Ni^{4+} redox processes, with no additional peaks, implying significant contributions from other redox reactions for Mn^{3+}/Mn^{4+} or Co^{3+}/Co^{4+} [31]. This was as expected within the selected voltage range [63]. These peaks showed a low polarization of 0.17 V at 0.1 mV s^{-1}, implying a highly reversible reaction. In contrast, at a scan rate of 0.5 mV s^{-1}, the peak separation grew to 0.35 V, which suggested the occurrence of an irreversible reaction could be responsible for the drop in capacity at higher rate cycling. This could have been due to the increased formation of the Solid Electrolyte Interface (SEI) or the Cathode Electrolyte Interface (CEI). The formation of carbon—oxygen species on the surface, due to the reaction of the organic electrolyte with the oxide surface, will lead to a permanent resistive layer [46]. This will lead to a greater charge transfer resistance, leading to a larger polarization of redox peaks.

All the samples showed well-defined CVs that were interrogated and the peak current, i_p, was plotted against the square root of scan rate ($v^{1/2}$) that allowed the lithium diffusion coefficient D, to be estimated via the Randles-Sevcik (R-S) equation [25].

$$i_p = 2.686 \times 10^5 n^{3/2} A D^{1/2} C v^{1/2}$$

The gradient of the fit plotted in the inset of Fig. 5a as well as the Li$^+$ concentration (C), the reaction electron count (n) and the electrode area (A), were used to determine D for each sample composition, plotted in ternary Fig. 5b). The trends in the R-S diffusion value vs composition map in Fig. 5b unsurprisingly, these follow closely with the percentage capacity retention plot at 1C in Fig. 4d. Higher Ni content led to a general increase in D, where a greater Co:Mn ratio led to the higher values still. This trend can be explained as being due to reduced cation mixing for samples in the high Ni, higher Co region, i.e. less Ni^{3+} blocking the intercalation channels for lithium, thereby lowering the resistance to Li$^+$ diffusion. Sample NMC 47:25:28 was calculated to have a R-S diffusion coefficient of 1.5×10^{-7} cm^2 s^{-1}, which was an order of magnitude greater than the NMC 34:34:33 sample (at 2.9×10^{-8} cm^2 s^{-1}). As shown in Fig. 4d), increased nickel content starting from NMC111 (with slightly more cobalt), led to the highest diffusion coefficients

observed. In contrast, compositions that were low nickel and high manganese, did not favour rapid lithium intercalation.

The R-S method provides a useful indication of properties to be expected, however, Electrochemical Impedance Spectroscopy (EIS) can be used as a more accurate measurement of the diffusion coefficient. Furthermore, by testing the impedance before and after rapid CV cycling, the effect of SEI or other phase formation could be measured by looking at the charge transfer resistance, R_{ct}. An example EIS Nyquist plot can be seen in Fig. 5c, with markers for the NMC 39:28:33 sample prior to CV cycling. Half cells were tested at open circuit voltage in their uncharged state. Useful numerical values can be extracted from the data using a lumped equivalent circuit; in this case, a typical Randle's circuit was used as shown in the inset of Fig. 5c [64]. Useful values extracted from the circuit include Resistance to Charge Transfer (R_{ct}) from the high frequency arc of the plot, and Warburg Impedance (Z_W), calculated from the linear region of the plot in the low frequency, arising from Li$^+$ bulk diffusion [19].

The values of pre-cycling R_{ct} and the % change after cycling ΔR_{ct}, measuring the resistance of electrode/electrolyte charge transfer, are displayed in Supplementary Figs. S4a and S4b, respectively. A large drop in resistance was seen in all samples after cycling, likely due to the formation of SEI, leading to a passivation of the electrode surface [19]. Several components in the SEI or degradation products have previously been reported in the literature for these changes, including surface Li$_2$CO$_3$, NiO rock salt or LiMn$_2$O$_4$ spinel [4,10,34]. In the work herein, surface Li$_2$CO$_3$ from the SEI could be responsible for the large R_{ct} observed from the NMC 39:28:33 sample. This would explain the initially high capacities and rapid capacity fade of the cathode as a result of possible surface species dissolution and/or corrosion [39]. Consistently, the NMC 35:36:29 sample had the lowest R_{ct} after cycling, which has previously been suggested to be due to the formation of a manganese rich spinel phase protecting the sample from thick SEI formation [65].

The diffusion coefficient can also be calculated using the Warburg constant σ, determined from the gradient of the slope of real impedance (Z Re) against the inverse root of frequency ω [41]. This is taken from the low frequency region as shown in the inset in Fig. 5c.

$$D = \frac{R^2 T^2}{2A^2 C^2 \sigma^2 n^4 F^4}$$

In this case R refers to the universal gas constant, T the temperature and F the Faraday constant (96,485 C/mol), the diffusion coefficients are plotted in D against composition. The values presented are ca. 4 orders of magnitude lower than those measured by CV, and are likely to be closer to the true bulk values of lithium diffusion coefficient. Somewhat surprisingly, the maxima in the plots do not appear to align with the constants determined by R-S calculation. However, the EIS values were determined after cycling at scan rates of up to 50 mV s^{-1}, whereas the linear relation for R-S against square root of the scan rate value, stopped after running at a scan rate of 5 mV s^{-1}. Perhaps the harsh cycling conditions used, could have led to side species formation that severely hindered the performance of some of the samples.

3. Conclusions

A library of near-NMC111 compositions was explored using a combined continuous hydrothermal precipitation plus solid state lithiation approach, to give sub-micron and phase pure $R\bar{3}m$ structures in all cases. The materials obtained were self-consistent, displaying graduated changes in properties for electrochemical and other data. This is a testament to the reproducible and consistent
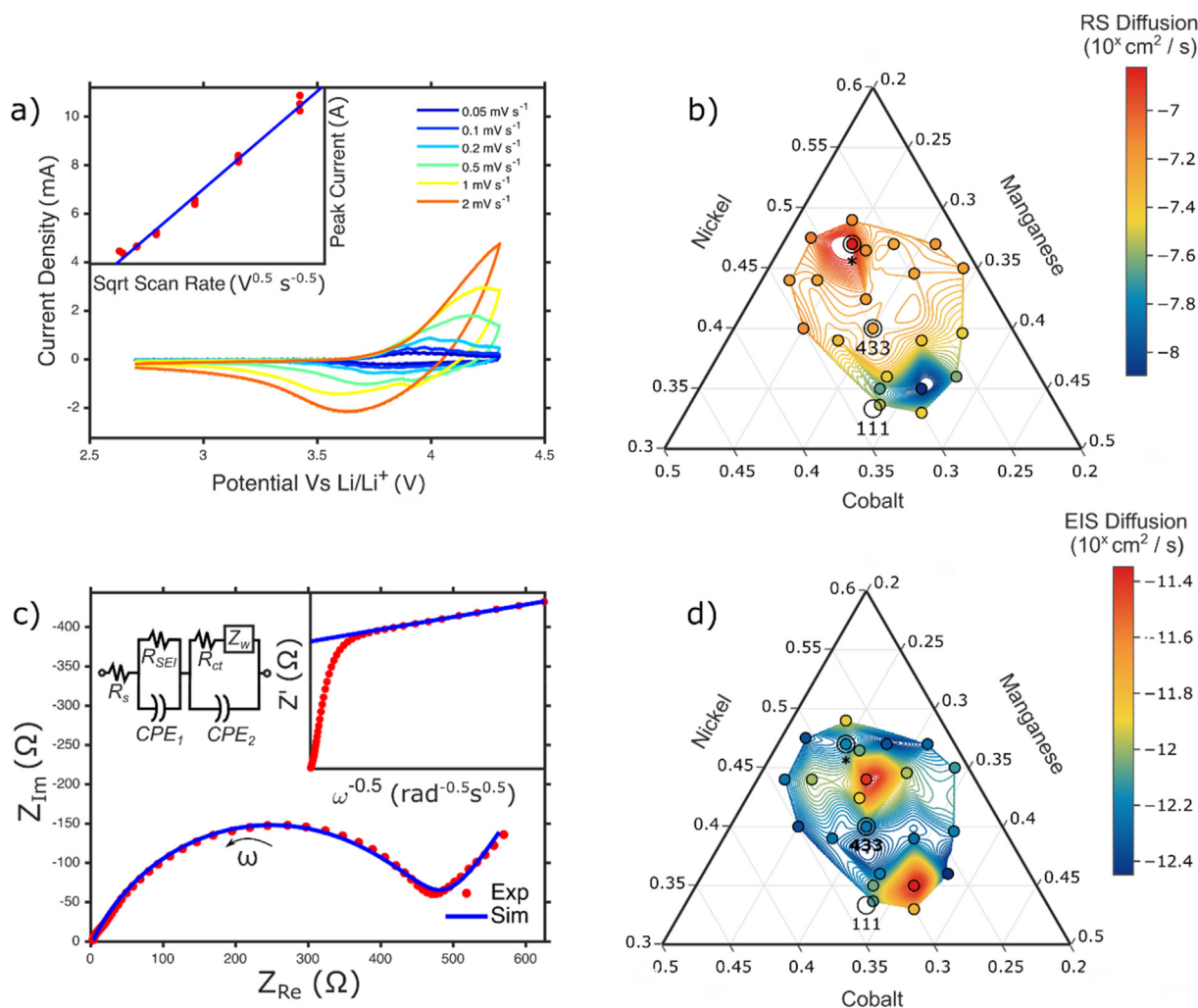
Fig. 5. a) Cyclic Voltammograms for the NMC 39:28:33 sample at a range of scan rates, with an inset plotting peak current against the root scan rate for the Randles-Sevcik (R-S) diffusion. b) Shows the R-S diffusion coefficient across compositional space. c) Shows the Electrochemical Impedance Spectrum (EIS) Nyquist plot for the pre-cycled NMC 39:28:33 sample; with insets showing equivalent circuit (left) and inverse root of frequency plotted against real impedance (right). d) Shows EIS diffusion coefficients plotted against compositional space. The high-power sample NMC 47:25:28 is highlighted by *.

synthesis approach adopted; the first step of synthesis allowed consistent and well mixed fine and homogenous precipitates to be quickly made, which, after solid state lithiation of samples, greatly aided comparison of the NMCs. For the high Ni content NMC materials in the library (e.g. samples NMC 47:25:28 and NMC 45:31:2), it was found that slightly increased ratio of Co:Mn, helped to reduce cation mixing in the active materials. SEM images of selected NMCs, revealed a primary particle size of ca. 300 nm in all the materials studied, within larger assembled microstructures. This was linked to the ability of some of these materials to retain a decent and stable capacity at high C rates. Some compositions showed improved electrochemical performance over near-NMC111 and NMC433 composition samples in Li-ion half-cells. The NMC 39:28:33 sample showed the greatest specific capacity and therefore, highest energy density at low C rates. In contrast, sample NMC 47:25:28 showed the greatest high rate capability (and highest power density) amongst all samples. Analysis of the CV and EIS data, allowed important trends in the form of compositional heatmaps for diffusion coefficients to be generated. Overall, this study was successful in providing a set of self-consistent data that will no doubt increase our understanding of the subtle interplay between structure-properties and composition. This could be an

invaluable tool for modellers to better predict high performance materials or developing those which are more environmentally sustainable and inexpensive.

4. Experimental methods

4.1. Synthesis

The precursor powder library of 23 precipitated samples (pre-solid-state lithiation) were synthesised in series using a Continuous Hydrothermal Flow Synthesis (CHFS) reactor, which incorporated a Confined Jet Mixer, CJM (patent no. US 9192901); see Scheme S1A in the supporting information. The CJM was designed to allow instant and highly turbulent mixing of an ambient temperature aqueous metal salt mixture with a superheated water feed, without any blockages. See Supplementary Scheme S1b for the design and specifications of the mixer used [66–68]. The CHFS process has been described at lab and pilot plant scales elsewhere in the literature [69,70]. A CHFS pilot plant was used in this work that has a design as follows; two identical high pressure pumps (Primeroyal K, Milton Roy, France) were used to deliver the aqueous metal feeds (pump P2) and the aqueous KOH base feed (pump P3), respectively.

D. Commandeur, C. Sabado, T.E. Ashton et al.

First the two ambient temperature feeds were mixed in flow in a dead volume tee mixer, prior to entering the CJM (both pumps at 200 mL min^{-1}; KOH feed 2 M; concentrations found in Table S1, with the total transition metal concentration = 0.4 M). Precursor purity and supplier can be found in the supporting information. A third pump (P1) was used to pump room temperature DI water under pressure at 400 mL min^{-1} into a heat exchanger at 450 °C. The combined P2 + P3 flow at ambient temperature was mixed in the CJM with the supercritical water flow, whereupon precipitation and crystallisation occurred (mixing temperature of 335 °C) [71–76]. Thereafter, the slurry was cooled in process after passing through a pipe-in-pipe heat exchanger. The sample slurry product was then collected at the exit of the CHFS process at ca. 50 °C, see Scheme S1 [77]. The collected slurry was then centrifuged (2 min at 4000 rpm) and the wet solids were cleaned by dialysis over 1 week until a conductivity value below 100 μS was achieved. The cleaned slurry was then centrifuged for 3 h at 4000 rpm (model Sigma 6-16S, Sigma Aldrich, Dorset, UK) into a thick paste and freeze-dried at 3×10^{-7} MPa for 20 h (Virtis Genesis 35XL, Biopharma process systems, Winchester, UK) to obtain a free flowing NMC precursor powder.

The freeze-dried NMC precursor powders were then lithiated using an incipient wetness type method. 2.0 g of each CHFS powder composition was saturated with the required amount of 5 M lithium hydroxide aqueous solution (Li was 30% excess) based on M_r (Table S1). The wet mixture was then homogenised using a Thinky™ mixer (model ARE-310) at 1000 rpm for 30 min using ten 3 mm zirconia balls. The resulting thick black slurry for each sample was then subsequently freeze-dried using a Virtis Genesis 35XL. Each of the powders were then gently dry ground at 1000 rpm for 10 min in the Thinky™ mixer with ten ZrO_2 balls.

Each of the 23 samples was then individually heat-treated in 4.2 cm wide zirconia crucibles in a box furnace (CWF1105-230SN-CWF, Carbolite, Derbyshire, UK) in air to form the corresponding phase pure $LiNi_xMn_yCo_zO_2$ samples. The samples were first heated to 800 °C for 8 h (ramp rate 3 °C min^{-1}) followed by 600 °C for 12 h (ramp rate 3 °C min^{-1}). Once when it cool, the samples were gently hand-ground prior to characterisation and electrode manufacture. All sample compositional labels hereafter were determined by X-ray Fluorescence (XRF) data rather than the nominal values.

4.2. Structural and physical characterisation

The samples were characterised by powder X-ray diffraction (PXRD) using a STOE StadiP diffractometer (Mo Kα radiation $\lambda = 0.7107$ Å), with a 2θ range from 5 to 40°, 0.5° step size and 20 s step time. The transition metal ratios were determined by XRF using an Epsilon 3 benchtop spectrometer (Malvern Panalytical Ag-anode 50 kV X-rays). Scanning electron microscopy was used to analyse sample morphology, using a JEOL JSM-6300 in secondary electron mode with Hitachi S−3400 N field emission instruments (20 kV).

4.3. Electrochemical characterisation

Cathodes were prepared by combining the lithiated samples with Super P conductive carbon (Alfa Aesar, Heysham, UK) followed by PVDF polymeric binder (polyvinyl fluoride, PI-KEM, Stafford-shire, UK) in the wt% ratio 80:10:10. The PVDF was dissolved beforehand in N-methyl-2-pyrrolidone (NMP, Sigma Aldrich, Dorset, UK) as a 5 wt% solution. The viscous slurry was mixed in a Thinky™ mixer for 10 min at 1000 rpm with ten ZrO_2 balls (3 mm), before doctor blading on aluminium foil. Once briefly dried for 10 min on a 110 °C hot plate, individual coin cell electrodes were punched out to 15 mm diameter and dried for 2 h under vacuum at 60 °C in the Ar-filled glove box (O_2 and H_2O < 0.1 ppm) antechamber before entry for cell assembly. The active mass loading was ~3 mg cm^{-2} and the electrode thickness was 150 μm. The half cells were assembled with a lithium foil (PI-KEM, Staffordshire, UK) counter electrode in CR2032 casings, using a glass microfibre separator (Whatman GF/D, Buckinghamshire, UK) cut to 20 mm diameter. This was saturated in 1 M $LiPF_6$ electrolyte with a 3:7 solvent weight ratio of ethylene carbonate:ethyl methyl carbonate (Targray, Canada).

An Arbin Instrument model BT-2000 (Caltest Instruments Ltd, Guildford, UK) was used to perform galvanostatic charge/discharge cycling at ~20 °C. Symmetric cycling tests used a potential range of 2.7–4.3 V vs Li/Li$^+$ with various C-rate tests of C/20, C/10, C/5, C/2, C and C/20. The specific capacities used to determine the current density at 1 C were scaled according to nickel content, included in Table S1. Cyclic voltammetry measurements used the same instrument and an identical potential window as galvanostatic charge/discharge, with scan rates of 0.05, 0.1, 0.2, 0.5, 1, 2, 5, 10, 20 and 50 mV s^{-1}. Electrochemical impedance spectroscopy was tested using an Interface 1000 Gamry potentiostat (Gamry Instruments, Pennsylvania, US), at a DC voltage bias of 0 V vs open circuit voltage and a sinusoidal AC voltage of 10 mV. Cells were tested in their discharged state before and after CV cycling, using a frequency range of 1 Hz to 1 MHz.

Declaration of competing interest

The authors declare no conflicts of interest.

Acknowledgements

Appendix A. Supplementary data

Supplementary data to this article can be found online at https://doi.org/10.1016/j.jmat.2021.07.003.

References

[1] Jun D-W, Yoon CS, Kim U-H, Sun Y-K. Chem Mater 2017;29:5048–52.
[2] Hwang S, Chang W, Kim SM, Su D, Kim DH, Lee JY, Chung KY, Stach EA. Chem Mater 2014;26:1084–92.
[3] Hwang K, Sohn H, Yoon S. J Power Sources 2018;378:225–34.
[4] Kim U-H, Myung S-T, Yoon CS, Sun Y-K. ACS Energy Lett 2017;2:1848–54.
[5] Barai P, Feng Z, Kondo H, Srinivasan V. J Phys Chem B 2019;123:3291–303.
[6] Chikkannanavar SB, Bernardi DM, Liu L. J Power Sources 2014;248:91–100.
[7] Ohzuku T, Ueda A, Nagayama M, Iwakci-hi Y, Komori H. Electrochim Acta 1993;38:1159–67.
[8] Goodenough JB, Park K-S. J Am Chem Soc 2013;135:1167–76.
[9] Gao S, Cheng Y-T, Shirpour M. ACS Appl Mater Interfaces 2019;11:982–9.
[10] Nohma T, Kurokawa H, Uehara M, Takahashi M, Nishio K, Saito T. J Power Sources 1995;54:522–4.
[11] Liu W, Oh P, Liu X, Lee MJ, Cho W, Chae S, Kim Y, Cho J. Angew Chem Int Ed 2015;54:4440–57.
[12] Li M, Lu J. Science 2020;367:979–80.
[13] Madec L, Petibon R, Xia J, Sun J-P, Hill IG, Dahn JR. J Electrochem Soc 2015;162:A2635–45.
[14] Röder P, Stiaszny B, Ziegler JC, Baba N, Lagaly P, Wiemhöfer HD. J Power Sources 2014;268:315–25.
[15] Zhang X, Luo D, Li G, Zheng J, Yu C, Guan X, Fu C, Huang X, Li L. J Mater Chem A 2013;1:9721.
[16] Ren D, Padgett E, Yang Y, Shen L, Shen Y, Levin BDA, Yu Y, Disalvo FJ, Muller DA, Abruña HD. ACS Appl Mater Interfaces 2019;11:41178–87.

D. Commandeur, C. Sabado, T.E. Ashton et al.

[17] Becker D, Börner M, Nölle R, Diehl M, Klein S, Rodehorst U, Schmuch R, Winter M, Placke T. ACS Appl Mater Interfaces 2019;11:18404−14.
[18] Lai Y, Wu J, Tang Y, Shang G, Yang X, Fan H, Peng C, Zhang Z. Ceram Int 2019;45:14270−7.
[19] Wise AM, Ban C, Weker JN, Misra S, Cavanagh AS, Wu Z, Li Z, Whittingham MS, Xu K, George SM, Toney MF. Chem Mater 2015;27:6146−54.
[20] Wang M, Zhang R, Gong Y, Su Y, Xiang D, Chen L, Chen Y, Luo M, Chu M. Solid State Ionics 2017;312:53−60.
[21] Julien C. Solid State Ionics 2000;135:121−30.
[22] Lin F, Markus IM, Nordlund D, Weng T-C, Asta MD, Xin HL, Doeff MM. Nat Commun 2014;5:3529.
[23] Gao S, Zhan X, Cheng Y-T. J Power Sources 2019;410−411:45−52.
[24] Xu X, Xiang L, Wang L, Jian J, Du C, He X, Huo H, Cheng X, Yin G. J Mater Chem A 2019;7:7728−35.
[25] Hou P, Li F, Sun Y, Li H, Xu X, Zhai T. ACS Appl Mater Interfaces 2018;10:24508−15.
[26] Gao P, Li Y, Liu H, Pinto J, Jiang X, Yang G. J Electrochem Soc 2012;159:A506−13.
[27] Noh HJ, Youn S, Yoon CS, Sun YK. J Power Sources 2013;233:121−30.
[28] Huang Z, Gao J, He X, Li J, Jiang C. J Power Sources 2012;202:284−90.
[29] Xie H, Du K, Hu G, Peng Z, Cao Y. J Phys Chem C 2016;120:3235−41.
[30] Guilmard M. J Power Sources 2003;115:305−14.
[31] Shao Y, Huang B, Lu Z, Liu Y, Meng X, Du L, Song H, Liao S. Energy Technol 2019;7:2−9.
[32] Wang GX, Zhong S, Bradhurst DH, Dou SX, Liu HK. Solid State Ionics 1999;116:271−7.
[33] Hy S, Liu H, Zhang M, Qian D, Hwang BJ, Meng YS. Energy Environ Sci 2016;9:1931−54.
[34] Cho Y, Lee S, Lee Y, Hong T, Cho J. Adv. Energy Mater. 2011;1:821−8.
[35] Shi J-L, Zhang J-N, He M, Zhang X-D, Yin Y-X, Li H, Guo Y-G, Gu L, Wan L-J. ACS Appl Mater Interfaces 2016;8:20138−46.
[36] Yu C, Li G, Guan X, Zheng J, Li L. Electrochim Acta 2012;61:216−24.
[37] Sun YK, Chen Z, Noh HJ, Lee DJ, Jung HG, Ren Y, Wang S, Yoon CS, Myung ST, Amine K. Nat Mater 2012;11:942−7.
[38] Zhao R, Chen Z, Zhang Y, Du P, Chen H. Mater Lett 2014;136:160−3.
[39] Pimenta V, Sathiya M, Batuk D, Abakumov AM, Giaume D, Cassaignon S, Larcher D, Tarascon JM. Chem Mater 2017;29:9923−36.
[40] Zhang Y, Li H, Liu J, Zhang J, Cheng F, Chen J. J Mater Chem A 2019;7:20958−64.
[41] Zheng J, Yan P, Estevez L, Wang C, Zhang J-G. Nanomater Energy 2018;49:538−48.
[42] Park KS, Cho MH, Jin SJ, Nahm KS, Hong YS. Solid State Ionics 2004;171:141−6.
[43] Yu C, Li G, Guan X, Zheng J, Li L. Electrochim Acta 2012;61:216−24.
[44] Rozier P, Tarascon JM. J Electrochem Soc 2015;162:A2490−9.
[45] Do SJ, Santhoshkumar P, Kang SH, Prasanna K, Jo YN, Lee CW. Ceram Int 2019;45:6972−7.
[46] Gao H, Cai J, Xu G-L, Li L, Ren Y, Meng X, Amine K, Chen Z. Chem Mater 2019;31:2723−30.
[47] Song B, Li W, Oh S-M, Manthiram A. ACS Appl Mater Interfaces 2017;9:9718−25.
[48] Ma M, Chernova NA, Toby BH, Zavalij PY, Whittingham MS. J Power Sources 2007;165:517−34.
[49] Yin L, Li Z, Mattei GS, Zheng J, Zhao W, Omenya F, Fang C, Li W, Li J, Xie Q, Erickson EM, Zhang J-G, Whittingham MS, Meng YS, Manthiram A, Khalifah PG. Chem Mater 2020;32:1002−10.
[50] Shen Z, Hu Y, Chen R, He X, Wu K, Cheng Z, Pan P, Jiang L, Mao J, Ni C. Nanoscale 2019;11:7744−53.
[51] Bauer D, Ashton TE, Brett DJL, Shearing PR, Matsumi N, Darr JA. Electrochim Acta 2019;322:134695.
[52] Griffith KJ, Wiaderek KM, Cibin G, Marbella LE, Grey CP. Nature 2018;559:556−63.
[53] Holzwarth U, Gibson N. Nat Nanotechnol 2011;6. 534−534.
[54] Ocakoglu K, Mansour SA, Yildirimcan S, Al-Ghamdi AA, El-Tantawy F, Yakuphanoglu F. Spectrochim Acta Part A Mol Biomol Spectrosc 2015;148:362−8.
[55] Tsai YZ, Wang NF, Tseng MR, Hsu FH. Mater Chem Phys 2010;123:300−3.
[56] V. J. Ovejas and A. Cuadras, Batteries, , DOI:10.3390/batteries4030043.
[57] Pişkin B, Uygur CS, Aydınol MK. Int J Hydrogen Energy 2020;45:7874−80.
[58] Cheng C, Tan L, Liu H, Huang X. Mater Res Bull 2011;46:2032−5.
[59] Lee K-S, Myung S-T, Amine K, Yashiro H, Sun Y-K. J Electrochem Soc 2007;154:A971.
[60] Huang B, Liu D, Qian K, Zhang L, Zhou K, Liu Y, Kang F, Li B. ACS Appl Mater Interfaces 2019;11:14076−84.
[61] Zhang B, Li L, Zheng J. J Alloys Compd 2012;520:190−4.
[62] Bak S, Hu E, Zhou Y, Yu X, Senanayake SD, Cho S, Kim K, Chung KY, Yang X, Nam K. Appl. Mater. Interfaces 2014;6:22594−601.
[63] Venkateswara Rao C, Leela Mohana Reddy A, Ishikawa Y, Ajayan PM. ACS Appl Mater Interfaces 2011;3:2966−72.
[64] Alavi SMM, Mahdi A, Payne SJ, Howey DA. IEEE Trans Contr Syst Technol 2017;25:2112−20.
[65] Pimenta V, Sathiya M, Batuk D, Abakumov AM, Giaume D, Cassaignon S, Larcher D, Tarascon J-M. Chem Mater 2017;29:9923−36.
[66] Weng X, Boldrin P, Abrahams I, Skinner SJ, Darr JA. Chem Mater 2007;19:4382−4.
[67] Powell MJ, Marchand P, Denis CJ, Bear JC, Darr JA, Parkin IP. Nanoscale 2015;7:18686−93.
[68] Gruar RI, Tighe CJ, Muir J, Kittler JT, Wodjak M, Kenyon AJ, Darr JA. RSC Adv 2012;2:10037−47.
[69] Gruar RI, Tighe CJ, Darr JA. Ind Eng Chem Res 2013;52:5270−81.
[70] Tighe CJ, Cabrera RQ, Gruar RI, Darr JA. Ind Eng Chem Res 2013;52:5522−8.
[71] Johnson ID, Ashton TE, Blagovidova E, Smales GJ, Lübke M, Baker PJ, Corr SA, Darr JA. Sci Rep 2018;8:4114.
[72] Bauer D, Roberts AJ, Patnaik SG, Brett DJL, Shearing PR, Kendrick E, Matsumi N, Darr JA. J Electrochem Soc 2018;165:A1662−70.
[73] Hu L, Johnson ID, Kim S, Nolis GM, Freeland JW, Yoo HD, Fister TT, McCafferty L, Ashton TE, Darr JA, Cabana J. Nanoscale 2019;11:639−46.
[74] Darr JA, Zhang J, Makwana NM, Weng X. Chem Rev 2017;117:11125−238.
[75] Malarde D, Johnson ID, Godfrey IJ, Powell MJ, Cibin G, Quesada-Cabrera R, Darr JA, Carmalt CJ, Sankar G, Parkin IP, Palgrave RG. J Mater Chem C 2018;6:11731−9.
[76] Denis CJ, Tighe CJ, Gruar RI, Makwana NM, Darr JA. Cryst Growth Des 2015;15:4256−65.
[77] Marchand P, Makwana NM, Tighe CJ, Gruar RI, Parkin IP, Carmalt CJ, Darr JA. ACS Comb Sci 2016;18:130−7.

Daniel Commandeur: As a research scientist, Daniel is fascinated by the application of novel materials to urgent real world problems such as renewable energy generation and storage. He completed his PhD at the University of Sussex in 2019, using zinc oxide nanowires to increase the efficiency of hydrogen generation via solar water splitting, along with building perovskite solar cells on them. From 2019 to 2021, Daniel worked on synthesising lithium ion cathode materials using continuous hydrothermal flow synthesis. This work involved improving the rate capability of said materials for improved high power performance. Currently, Daniel works as a research fellow at the University of Surrey, investigating polymer membranes and carbon electrodes for supercapacitors.

Jawwad Darr: Research with Prof Darr's Clean Materials Technology Group, is concerned with the application of green principles and clean technologies for the rapid and efficient syntheses of nanoparticles or new inorganic materials. The research is very applied and multidisciplinary covering chemistry, nanomaterials, high pressure engineering, flow reactors, scale-up, supercritical fluids and automation.